PHYSICAL REVIEW E **77**, 061902 (2008)

Shape of nonseptated *Escherichia coli* is asymmetric

E. Itan,[1,2] G. Carmon,[1,2] A. Rabinovitch,[1] I. Fishov,[3] and M. Feingold[1,2]
[1]*Department of Physics, Ben Gurion University, Beer Sheva 84105, Israel*
[2]*The Ilse Katz Center for Nanotechnology, Ben Gurion University, Beer Sheva 84105, Israel*
[3]*Department of Life Sciences, Ben Gurion University, Beer Sheva 84105, Israel*

(Received 4 October 2007; revised manuscript received 19 March 2008; published 4 June 2008)

The shape of *Escherichia coli* is approximately that of a cylinder with hemispherical caps. Since its size is not much larger than optical resolution, it has been difficult to quantify deviations from this approximation. We show that one can bypass this limitation and obtain the cell shape with subpixel accuracy. The resulting contours are shown to deviate from the hemisphere-cylinder-hemisphere shape. In particular, the cell is weakly asymmetric. Its two caps are different from each other and the sides are slightly curved. Most cells have convex sides. We discuss our results in light of several mechanisms that are involved in determining the shape of cells.

DOI: 10.1103/PhysRevE.77.061902 PACS number(s): 87.57.N−, 87.18.−h, 87.16.Gj

I. INTRODUCTION

The envelope of Gram-negative bacteria, e.g., *Escherichia coli* (*E. coli*), consists of three layers: the cytoplasmic membrane (CM), the peptidoglycan, and the outer membrane (OM). Next to the cytoplasm lies the CM, a phospholipid bilayer that forms the main permeability barrier. The outer membrane is also a bilayer. It contains phospholipids on the inside and lipopolysaccharides on its outside. The peptidoglycan cell wall, the sacullus, is located in the gap between the two membranes, the periplasmic space, and is linked to the OM by lipoproteins. It is stiff and therefore determines the shape of the cell. *In vitro* measurements of hydrated sacculi of *E. coli* using atomic force microscopy (AFM) found that these are about 6 nm thick [1]. Their elastic modulus, E, was also measured [1]. It is larger along the hoop, E_ϕ, than in the axial direction, E_z. On average, $E_\phi = 4.5 \times 10^7\ \mathrm{N/m^2}$ and $E_z = 2.5 \times 10^7\ \mathrm{N/m^2}$. Since the cell exerts a large turgor pressure on its wall, between 3 and 5 atm [2–4], the stiffness of the sacculus is necessary in order to contain it. During growth, the sacculus is also required to maintain the rod shape of the cell. Although it fulfills the shape maintenance task with good accuracy, some deviations from the hemisphere-cylinder-hemisphere configuration can be found in *E. coli* in the exponential phase. In this work, we present a detailed characterization of this shape variability for cells that have not yet developed a visible septum. Such quantitative information sets some constraints on the mechanisms that play a role in determining the shape of *E. coli*. We discuss several such mechanisms in light of our results.

The peptidoglycan envelope grows differently in the various parts of the cell [5,6]. While the old caps are inert, the cylindrical portion and the septum are generated by different peptidoglycan factories. The cylinder is grown by a network dependent on Penicillin Binding Protein 2 (PBP2). On the other hand, the formation of the septum was shown to depend on both PBP2 and PBP3 [7,8]. Along the cylinder, PBP2 is localized on patches that appear to be randomly distributed [7,9]. Since there are on average around a few tens of PBP2 molecules per cell [10] and the corresponding number of patches is necessarily smaller, deviations from uniformity in the patch distribution may lead to deviations from the rod shape. For example, banana-shaped cells may result from an excess of peptidoglycan forming patches on one side of the cell relative to the other. However, we find that such cells are rare and that most cells have convex sides. This suggests that randomly distributed growth foci alone cannot determine the shape of the *E. coli* cell. Additional or alternative mechanisms are required. The primitive bacterial cytoskeleton is a leading candidate for such a mechanism.

In most rod-shaped bacteria, the actin-like MreB protein together with the tubulinlike FtsZ were shown to form a cytoskeletal-like structure [11]. The MreB organize in helical filaments beneath the CM and *mreB* mutants display deformed or lytic phenotypes. MreB is believed to colocalize with the PBP2 peptidoglycan factories. Its role in *B. subtilis* where it cooperates with Mbl was studied using fluorescent vancomycin (Van-Fl, vancomycin is a cell wall synthesis inhibitor that binds specifically to peptidoglycan intermediates). Less is known about the action of MreB in *E. coli*. Here Mbl is absent and Van-Fl does not penetrate the outer membrane. Nevertheless, YFP-MreB filaments were reported to change their organization during the cell cycle forming helical structures along the long cell axis and/or single loops or rings at midcell [12]. The MreB filaments may play an important role in determining the shape of *E. coli* by coordinating the spatial organization of the peptidoglycan growth centers. Alternatively, the helical MreB structure may simply form the skeleton onto which peptidoglycan is constrained to grow independently on where the new peptidoglycan strands are inserted.

Our analysis of cell geometries cannot resolve the MreB dependent mechanism that participates in molding the cell shape of *E. coli*. On the other hand, it suggests that turgor pressure, P_t, may also play a role in determining cell shapes. Turgor pressure is closely related to the osmolality of the growth medium, Osm, and the corresponding osmotic pressure. For *E. coli*, it was shown that P_t decreases from ~3 atm at vanishing Osm to ~0.5 atm at 0.8 Osm [13]. At larger osmolalities of the medium, cells undergo plasmolysis whereby the CM caves in, detaching from the cell wall. The effect of osmotic pressure on the bacterial cell properties has been studied extensively in the past. While the cell volume was found to decrease with Osm, cell buoyant density grows as Osm increases [14]. Moreover, in osmotic shock experiments, where cells are grown at a given Osm, Osm_1, and then moved to new medium with a different Osm, Osm_2, it was shown that the cell volume and density take values that are different from those at both Osm_1 and Osm_2 [15]. In similar osmotic shock experiments, we find that the curvature of the cell sides decreases with increasing osmolality of the medium. No such trend is observed in experiments where cells are grown at different osmolalities. This could be because in such experiments other cell properties are changing, and some of them have their own influence on the behavior of cell curvature.

Since the width of *E. coli* is not much larger than the optical resolution, the deviations from the rod shape could not be quantified using optical microscopy. On the other hand, electron microscopy images of bacterial cells are likely to be distorted by sample preparation artifacts. We show that a careful analysis of fluorescence and phase contrast images can be used to bypass this barrier. Calibrating the pixel intensities, we are able to locate the edge of single cells with subpixel precision. We find that nonseptated cell shapes deviate from that of a cylinder with hemispherical caps. In particular, cells are asymmetric with respect to both their long and short axes. Their two caps have different radii and the long sides are weakly curved.

II. EXPERIMENTAL METHODS

A. Microscopy

Imaging experiments are performed on an inverted Olympus microscope (IX70). For bright-field and phase-contrast illumination, it is equipped with a halogen lamp located above the sample (transmission mode). A mercury lamp provides epi-illumination for fluorescence microscopy. An oil immersion 100× objective (UPLFLN 100XO2PH, 1.3NA) was used in all experiments. Images were captured with a Micromax camera (Roper). It has a 512×512 chip where the pixel is $13\ \mu\mathrm{m}\times13\ \mu\mathrm{m}$ and is cooled to $-20°$. The camera was synchronized with two computer-controlled shutters (Uniblitz). One shutter blocks the mercury lamp and the other the halogen lamp. This allows us to illuminate the sample only during the camera exposure time. Moreover, switching between phase contrast and fluorescence imaging modes is remotely controlled.

In our optical system, the pixel size corresponds to a length of 87 nm. This was calibrated using a micrometer ruler (Zeiss) with a 10 μm division. It was imaged in phase-contrast. Several tests where performed to estimate the magnitude of optical abberations. First, we divided the CCD field of view ($44\ \mu\mathrm{m}\times44\ \mu\mathrm{m}$) into a 3×3 square grid and measured the distance between two consecutive markings of the ruler, D, in each of the squares. D was measured with subpixel precision in both x and y directions, D_x and D_y, respectively. The difference between the average D_x and D_y is 0.3% and the individual measurements of D_x fluctuate by less than that (same for D_y). These differences are less than the corresponding measurement error, which is 0.7% (70 nm).

The constancy of distances over the field of view was also tested for the case of fluorescent imaging. We used fluorescently coated beads of 0.1 μm diameter (Polysciences) that were fixed to the coverslip. A pair of beads were located along the x axis $d_x=4.92\ \mu\mathrm{m}$ apart. A second pair was positioned along the y axis at a distance $d_y=3.97\ \mu\mathrm{m}$ from each other. We moved the two pairs along a 4×4 square grid scanning the CCD field of view and measured the distance between the beads at each location. Bead locations were measured using the symmetry algorithm that is accurate within less than 2 nm [16]. We found that both d_x and d_y are practically constant. Specifically, $\mathrm{Sd}(d_x)=6.1$ nm and $\mathrm{Sd}(d_y)=5.9$ nm, where Sd denotes the standard deviation.

The 0.1 μm fluorescent beads where also used to characterize the point spread function (PSF). We found that the widths in the x and y directions of the best-fitting two-dimensional (2D) Gaussian to the measured intensity distribution, σ_x and σ_y, are equal within experimental error. Due to imperfect control of the focus position, using the PSF to probe the uniformity of imaging over the field of view is not as accurate as the other tests. The possibility of optical artifacts in cell imaging itself was also analyzed and is discussed at the end of this section.

To measure cell shapes, we compare images in phase contrast and fluorescence that were taken at 1 s intervals. In the following, we show that correlating the information from the two images and using interpolation of the pixel intensities allows us to locate the CM with 22 nm accuracy.

B. Sample preparation

For our measurements, we use wild type *E. coli* B/r A that were grown in LB medium (10 g of tryptone, 5 g of yeast extract, 10 g of NaCl per liter). Monitoring the OD_{600}, we find that in LB the generation time is 26.0 ± 3.7 min. Moreover, to establish whether the bacterial culture is in the exponential growth regime, we have measured the distribution of cell sizes, $P(V)$, using a Coulter Counter (ZM, Coulter Electronics LTD). $P(V)$ was measured at different times corresponding to the range of OD_{600} between 0.1 and 0.33 and was found to be constant aside from experimental fluctuations. Finally, for several individual cells we have monitored the dynamics of their length throughout the cell life cycle, $L(t)$. We find the same growth law that we have observed in previous work [17]. In particular, a clear change in the rate of growth occurs at the start of division.

At $\mathrm{OD}_{600}=0.2$ in the exponential growth regime, cells were fixed in 1% formaldehyde and their cytoplasmic membrane (CM) was fluorescently stained with FM4-64 (molecular probes). For microscopy, 10 μL of the fixed and stained cells are pipetted onto a thin layer of 1.5% agar with LB. The sample is then covered with a coverslip and turned over for observation. In this configuration, cells are attached to a ceiling of agar laying on top of a 10 μm layer of LB solution. Experiments on live cells were also performed under the same conditions omitting the fixation and staining parts of the protocol. Since agar is about 10^3 softer than the cell walls of *E. coli* [1,18], it cannot affect its shape dynamics.

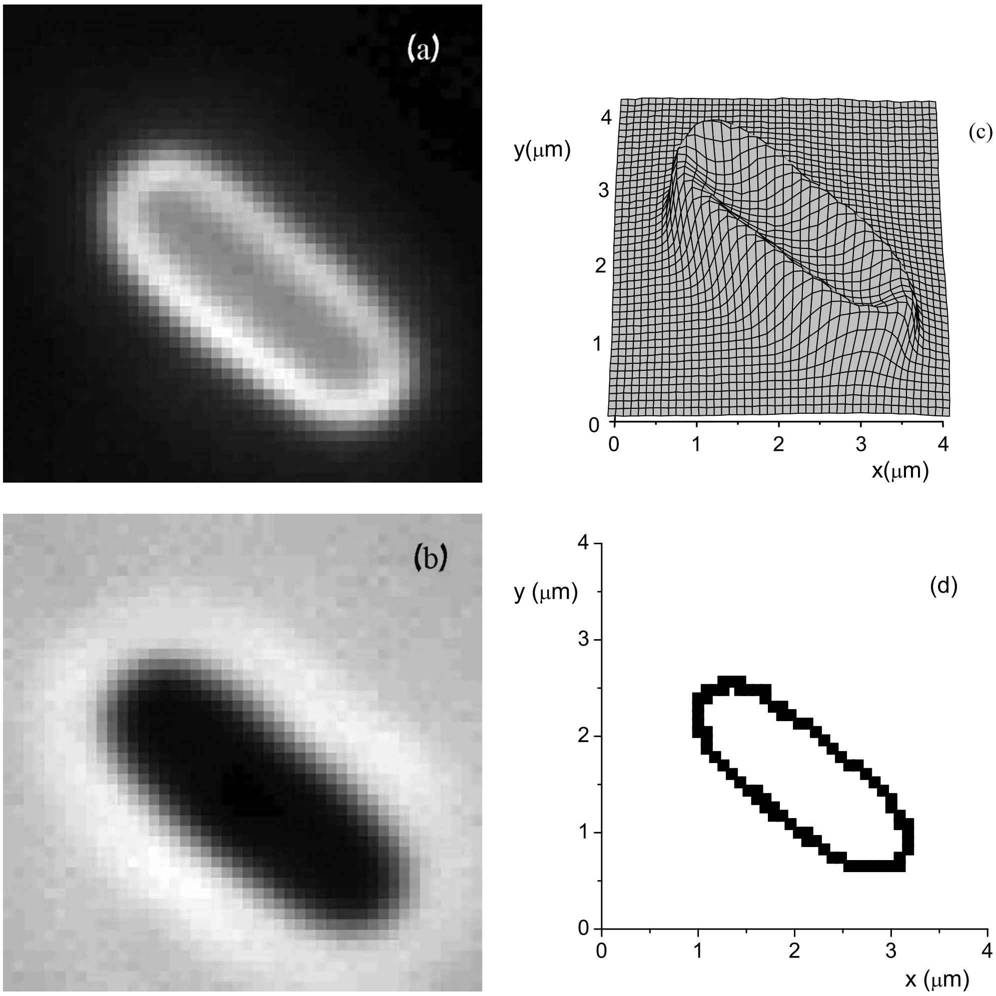

FIG. 1. Image of an individual *E. coli* cell. (a) The fluorescence image; (b) the phase-contrast image; (c) the intensity distribution in (a), $I_{\rm fl}$; (d) the zero approximation fluorescence contour; $\mathcal{C}_{\rm fl,0}$ (squares). The symbols are of the same size as that of the pixel. (a), (b), (c), and (d) have all the same scale and origin (the origin of the images lies in the lower left corner).

We use a population of 30 cells for the calibration of the method and a different population of 100 cells for shape measurements.

C. Notation

In what follows, we denote the contours that correspond to the cell edge as $\mathcal{C}$. Moreover, subscripts specify the method that was used to obtain a particular contour. We distinguish between contours that are measured from fluorescence images, $\mathcal{C}_{\rm fl}$, [see Figs. 1(a), 1(d), 2(e), and 2(f)], and those obtained from phase-contrast images, $\mathcal{C}_{\rm ph}$, [see Figs. 1(b), 2(e), and 2(f)]. Both $\mathcal{C}_{\rm fl}$ and $\mathcal{C}_{\rm ph}$ have been computed at two levels of accuracy. At the lowest level, the zero approximation, the error is of the order of one pixel and the corresponding contours are denoted as $\mathcal{C}_{\rm fl,0}$ [see Fig. 1(d)] and $\mathcal{C}_{\rm ph,0}$. The more accurate version of these contours is regarded as the first approximation and correspondingly denoted as $\mathcal{C}_{\rm fl,1}$ and $\mathcal{C}_{\rm ph,1}$ [see Figs. 2(e) and 2(f)]. The experimental errors for $\mathcal{C}_{\rm fl,1}$ and $\mathcal{C}_{\rm ph,1}$ are 22 and 31 nm, respectively.

Similarly, we denote the intensities in the fluorescence and phase-contrast images as $I_{\rm fl}$ and $I_{\rm ph}$, respectively. For phase-contrast images, we normalize the intensities such that, on average, the background has the value unity while the inside of the cell corresponds to zero. The normalized values of $I_{\rm ph}$ are denoted as $\tilde{I}_{\rm ph}$. The phase-contrast intensity threshold that on average corresponds to the cell edge is denoted by $\tilde{I}_{\rm th}$.

D. Finding the edge of the cell

In the fluorescence image, the position of the CM is well defined, namely, it corresponds to the ridge, $\mathcal{C}_{\rm fl}$, along which fluorescence intensity, $I_{\rm fl}$, is maximal [see Figs. 1(a) and 1(c)]. However, mainly due to staining inhomogeneity, $I_{\rm fl}(\mathcal{C}_{\rm fl})$ is not constant. In order to circumvent this problem, we developed an iterative, three-step approach for locating $\mathcal{C}_{\rm fl}$ that uses the corresponding phase-contrast image as a guide. An important by-product of our method is a threshold intensity value for the phase-contrast image that can be used to determine the location of the CM in similar cells independently of the fluorescence data. The three steps are as follows:

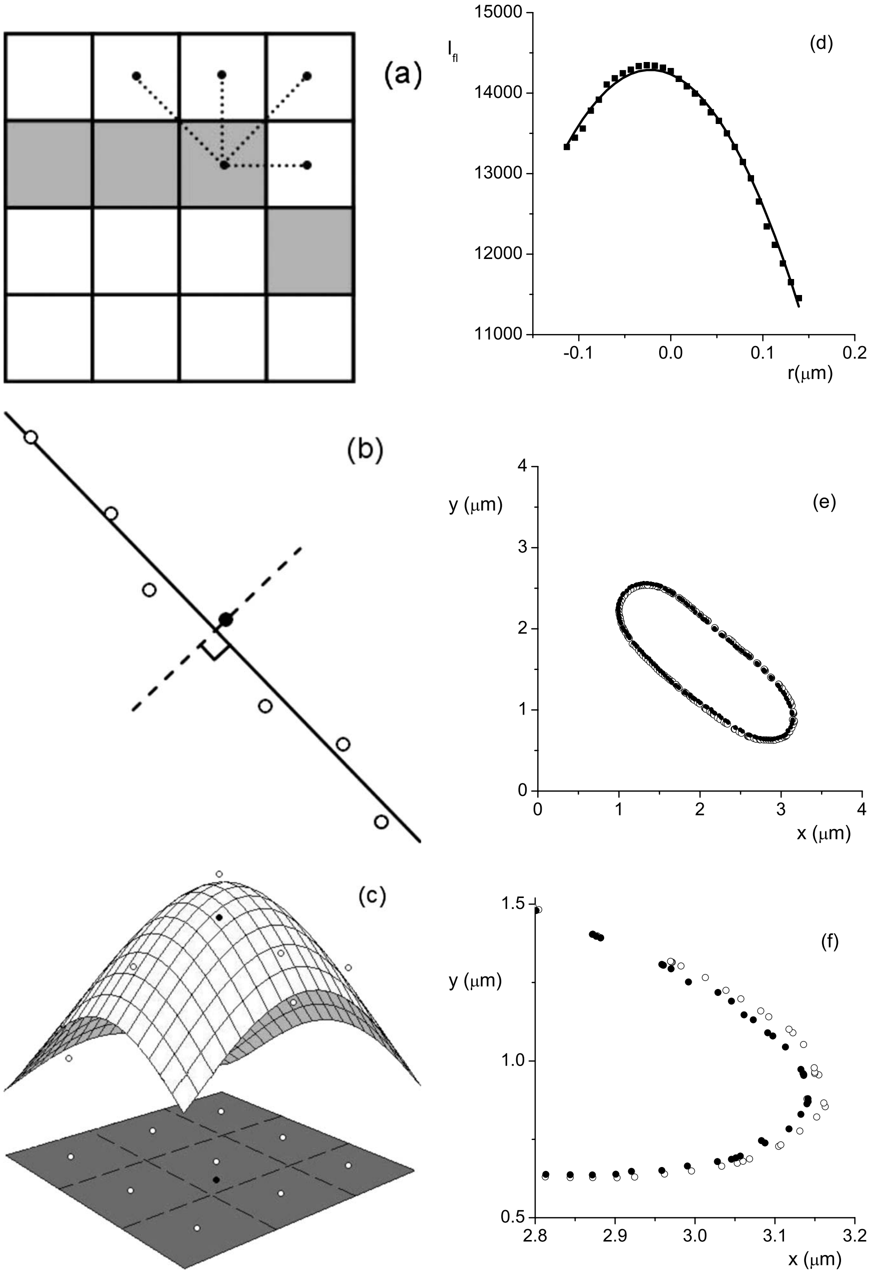

FIG. 2. The steps of the contour finding algorithm. (a) To find $\mathcal{C}_{\text{ph},0}$, we use linear interpolation between the pixels at the border of the interior, $\tilde{I}_{\text{ph}}<\tilde{I}_{\text{th},0}$ (gray), and those at the border of the exterior, $\tilde{I}_{\text{ph}}>\tilde{I}_{\text{th},0}$ (white), along the dashed segments (illustration). (b) Neighboring contour points of $\mathcal{C}_{\text{ph},0}$ (circles) are used to approximate the tangent and the ray at each contour point of $\mathcal{C}_{\text{ph},0}$ (full circle) (illustration). (c) A parabolic surface is used to fit the local I_{fl} data (open circles). The best-fitting surface is used to estimate I_{fl} at the point of interest along a particular ray (full circle) (illustration). (d) The distribution of fluorescence intensity values, I_{fl}, along a particular ray (squares), and the corresponding best-fitting parabola (line). (f) The first approximation fluorescence and phase-contrast contours, $\mathcal{C}_{\text{fl},1}$ (open circles) and $\mathcal{C}_{\text{ph},1}$ (full circles), respectively. (e) Enlarged view of the cap region in (e). (d), (e), and (f) correspond to the cell of Fig. 1.

(i) Find a first approximation to $\mathcal{C}_{\text{fl}}$ by choosing the maximal I_{fl} value and then moving clockwise to the next neighbor with the largest I_{fl} value until you obtain a closed curve, $\mathcal{C}_{\text{fl},0}$ [see Fig. 1(d)].

(ii) Calculate the average of the phase-contrast intensity along $\mathcal{C}_{\text{fl},0}$ to obtain the representative value that corresponds to the cell edge, $\tilde{I}_{\text{th},0}$. Use linear interpolation to obtain the contour in the phase-contrast image that corresponds to this threshold, $\mathcal{C}_{\text{ph},0}$ [see Fig. 2(a)].

(iii) Use $\mathcal{C}_{\text{ph},0}$ to obtain a better approximation for $\mathcal{C}_{\text{fl}}$. Define rays that pass through the points of $\mathcal{C}_{\text{ph},0}$ and are perpendicular to it [see Fig. 2(b)]. Use 2D quadratic interpolation to estimate I_{fl} at equidistant points along this ray [see Fig. 2(c)]. Finally, use 1D quadratic interpolation along the ray to estimate the position of maximal I_{fl}, $\mathcal{C}_{\text{fl},1,i}$ [see Fig. 2(d)]. These points, $\mathcal{C}_{\text{fl},1,i}$, form the first-order approximation to $\mathcal{C}_{\text{fl}}$, $\mathcal{C}_{\text{fl},1}$ [see Figs. 2(e) and 2(f)].

The first two steps of this method have been used before [17]. The result of step (i), $\mathcal{C}_{\mathrm{fl},0}$, is accurate within about one pixel. In step (ii), we first normalize the pixel intensities of each phase-contrast cell image such that the interior intensity is on average 0 and the exterior background is unity. We denote the normalized intensities as $\tilde{I}_{\mathrm{ph}}$. The average value of $\tilde{I}_{\mathrm{ph}}$ along $\mathcal{C}_{\mathrm{fl},0}$ and over 30 different cells, $\tilde{I}_{\mathrm{th},0}=0.26$, is the threshold intensity that approximately corresponds to the cell edge. We use linear interpolation between the pixel intensities on the two sides of the threshold in the phase-contrast image, $\tilde{I}_{\mathrm{ph}}$, to obtain $\mathcal{C}_{\mathrm{ph},0}$. The interpolation is performed between each pixel on the interior of the contour and its exterior closest neighbors [see Fig. 2(a)].

In the third step, to obtain a one-to-one correspondence between the points of $\mathcal{C}_{\mathrm{ph},0}$ and $\mathcal{C}_{\mathrm{fl},1}$, we search for the points of $\mathcal{C}_{\mathrm{fl},1}$ along rays perpendicular to $\mathcal{C}_{\mathrm{ph},0}$ at each of its contour points, $\mathcal{C}_{\mathrm{ph},0,i}$. These rays are obtained using a set of seven consecutive contour points of $\mathcal{C}_{\mathrm{ph},0}$, $\mathcal{C}_{\mathrm{ph},0,i+j}$ where $-3\leq j\leq 3$, centered on the contour point through which the ray passes, $\mathcal{C}_{\mathrm{ph},0,i}$ [see Fig. 2(b)]. The best-fitting line through the seven points is used to approximate the tangent to $\mathcal{C}_{\mathrm{ph},0}$ at $\mathcal{C}_{\mathrm{ph},0,i}$. The ray is perpendicular to the approximate tangent passing through $\mathcal{C}_{\mathrm{ph},0,i}$.

Along the rays we compute the fluorescence intensity I_{fl} at points P_i that are 0.1 pixel apart [see Fig. 2(d)]. The P_i points scan a range centered around the maximum fluorescence intensity. This range extends between the points where I_{fl} has decreased to $\frac{2}{3}$ of its maximal value relative to the background on the outer side of the cell and relative to the inner fluorescence intensity on the inside. The fluorescence values at P_i, $I_{\mathrm{fl}}(P_i)$, are estimated using 2D quadratic interpolation. Namely, for each P_i, we fit a 2D paraboloid to the measured fluorescence values of the nine neighboring pixels including the pixel to which the point belongs [see Fig. 2(c)]. Then, $I_{\mathrm{fl}}(P_i)$ are calculated from the value of the best-fitting paraboloid at P_i. To find the position of $\mathcal{C}_{\mathrm{fl},1}$ along a particular ray, we use 1D quadratic interpolation, fitting a parabola to $I_{\mathrm{fl}}(P_i)$ [see Fig. 2(d)]. The contour point of $\mathcal{C}_{\mathrm{fl},1}$, $\mathcal{C}_{\mathrm{fl},1,i}$, corresponds to the maximum of the best-fitting parabola.

In order to obtain a phase-contrast contour that has a similar accuracy to that of $\mathcal{C}_{\mathrm{fl},1}$, we reiterate step (ii) to obtain $\mathcal{C}_{\mathrm{ph},1}$. That is, we compute an improved value of the phase-contrast edge threshold by averaging the value of the phase-contrast intensity along $\mathcal{C}_{\mathrm{fl},1}$. To further improve accuracy, we use the estimated value of $\tilde{I}_{\mathrm{ph}}$ at the contour points of $\mathcal{C}_{\mathrm{fl},1}$ as obtained from linear interpolation. That is, the phase-contrast intensities from the three pixels closest to $\mathcal{C}_{\mathrm{fl},1,i}$ are used to define a 2D plane. The value of this planar surface at $\mathcal{C}_{\mathrm{fl},1,i}$ is used to obtain the average of $\tilde{I}_{\mathrm{ph}}$ along $\mathcal{C}_{\mathrm{fl},1}$. For the 30 cells used in the calibration, this leads to $\tilde{I}_{\mathrm{th},1}=0.24$, which is used to obtain $\mathcal{C}_{\mathrm{ph},1}$ in the same way as in step (ii) [see Figs. 2(e) and 2(f)].

E. The error of $\mathcal{C}_{\mathrm{fl},1}$

To estimate the error in the location of the contour points of $\mathcal{C}_{\mathrm{fl},1}$, we compare the estimated fluorescence values along the rays, $I_{\mathrm{fl}}(P_i)$, with the corresponding best-fitting parabolas. Since the fluorescence values vary significantly over the region of the fit, we average the relative deviation of the parabolic fit from the “data” points, $I_{\mathrm{fl}}(P_i)$, that were obtained from the 2D interpolation,

$$\delta I_{\mathrm{fl}} = \left\langle \frac{|I_{\mathrm{fl}}(P_i) - I_{\mathrm{fit}}(P_i)|}{I_{\mathrm{fl}}(P_i)} \right\rangle, \tag{1}$$

where $\langle\cdots\rangle$ denotes the average over the ray points, P_i. Then, the absolute error in the fluorescence value on the contour, ΔI_{fl}, is

$$\Delta I_{\mathrm{fl}}(\mathcal{C}_{\mathrm{fl},1,i}) = \delta I_{\mathrm{fl}} I_{\mathrm{fl}}(\mathcal{C}_{\mathrm{fl},1,i}). \tag{2}$$

To translate the error in intensity into the error in the position of $\mathcal{C}_{\mathrm{fl},1,i}$, we use the curvature of the fitted parabola, a, such that

$$\Delta\mathcal{C}_{\mathrm{fl},1,i} = \sqrt{\frac{\Delta I_{\mathrm{fl}}(\mathcal{C}_{\mathrm{fl},1,i})}{a}}. \tag{3}$$

The average value of $\Delta\mathcal{C}_{\mathrm{fl},1,i}$ over all the points of $\mathcal{C}_{\mathrm{fl},1}$ for the 30 cells used is 22 nm.

F. Further testing for optical and preparation artifacts

Our optical setup would be more accurate if a water immersion objective were used instead of our oil immersion objective. The ~10 μm LB layer between the coverslip and the cell will lead to optical abberations in cell imaging. On the other hand, there are no 100× water immersion objectives. We have compared a 60× water immersion objective (UPlanSApo, 1.2NA) to an analogous oil immersion (UPlanFl, 60×, 1.25NA) one in the context of our experiments. To this end, several fixed and FM-stained *E. coli* cells were fluorescence imaged with both objectives. The corresponding contours were obtained using a simplified version of our algorithm whereby instead of the lacking phase-contrast contour, $\mathcal{C}_{\mathrm{ph},0}$, we use $\mathcal{C}_{\mathrm{fl},0}$. Due to the lower magnification and the less accurate algorithm, the resulting contours are more noisy than the typical $\mathcal{C}_{\mathrm{fl},1}$ contours. Nevertheless, overlaying the two contours corresponding to a particular cell shows that they are equivalent up to experimental fluctuations.

A more accurate test of the effect of optical aberrations on our measurement was performed imaging a particular cell at 16 different locations over the entire CCD field of view. The corresponding contours, $\mathcal{C}_{\mathrm{ph},1}$, were analyzed leading to asymmetry parameters, averages of the ratio between the caps radii and curvatures of the long sides, that were constant aside from experimental fluctuations. These fluctuations had practically the same Sd’s as those obtained in the simulations of the rod shape with experimental noise presented in the next section. This indicates that these fluctuations are due to experimental error. Moreover, we found that there is no correlation between the fluctuations in the asymmetry parameters of the cell and the distance between the optical axis to the location where it was imaged. Finally, the different contour pairs were compared by translating one of them to the position where they were at a minimal total distance from each other. Following the translation, we found that up to small fluctuations the contours were equivalent. In particular, the average distance between all contour pairs is 16 nm, smaller than our experimental error.

Although fixation is not a necessary component in our experiments, it simplifies the experimental procedure. Using live cells requires preparing many samples in order to obtain the required statistics. In individual samples, due to growth, we obtain cells that have divided since sample preparation but continue to be in close proximity to each other. In such cases, the two daughter cells cannot be separated and analyzed by our algorithm. To establish that fixation and staining do not perturb the shape of the cells, we compared such cells to live ones under the same conditions. We find that the two populations display values of the parameters, length, width, and asymmetry parameters that are equal within experimental error.

One of our findings is that for individual cells, the two caps are not identical. This could be an artifact that results from cells not lying horizontally with respect to the optical axis. It may lead to cell images that are partially defocused such that one end of the cell appears different from the other. We have tested this possibility and obtained evidence that partial defocusing is not the reason for the measured asymmetry. In phase contrast, a focused image is sharply defined, that is, it gives a well-defined boundary between the inside of the cell and the surrounding background. This sharpness will manifest as a maximal intensity gradient at the cell edge. We have measured this gradient and compared its average value at each of the two caps of individual cells. We find that there is no apparent correlation between the measured left-right cell asymmetry and the difference between the gradients at the two cell caps. This suggests that the left-right asymmetry that we observe is not due to the angle at which cells lie on the agar substrate.

III. EXPERIMENTAL RESULTS

While the cell envelope is three-dimensional (3D), we only obtain a 2D projection of it (see Sec. II). The contour that we measure represents the edge of this projection and may be assumed to be equivalent to that of the corresponding equatorial section through the cell. Although this contour only provides partial information on the 3D envelope, we will refer to it as the shape of the cell.

The cell shapes that we find vary. Many are very close to a perfect rectangle with semicircular caps. Some, however, have unequal caps or caps that are slightly different from circular. As a result, the two sides of the cell are nonparallel and the left-right symmetry is broken. In addition, it is often the case that the sides display a weak curvature that is typically different between the two sides of the same cell. This breaks the cylindrical symmetry of the cell. Thus we observe cells that are either bi-convex (see Fig. 3), plano-convex (see Fig. 4), or convex-concave see (Fig. 5). We refer to the first as *fat* cells, the second as *half-fat*, and the latter as *banana* cells. We note that concave-concave cells cannot be clearly distinguished from septated cells and are therefore excluded from the population. Moreover, cell sides with curvatures smaller than a certain threshold determined by experimental error are classified as straight (see Fig. 4). The value of the minimal significant curvature was estimated using a numerical model (see below).

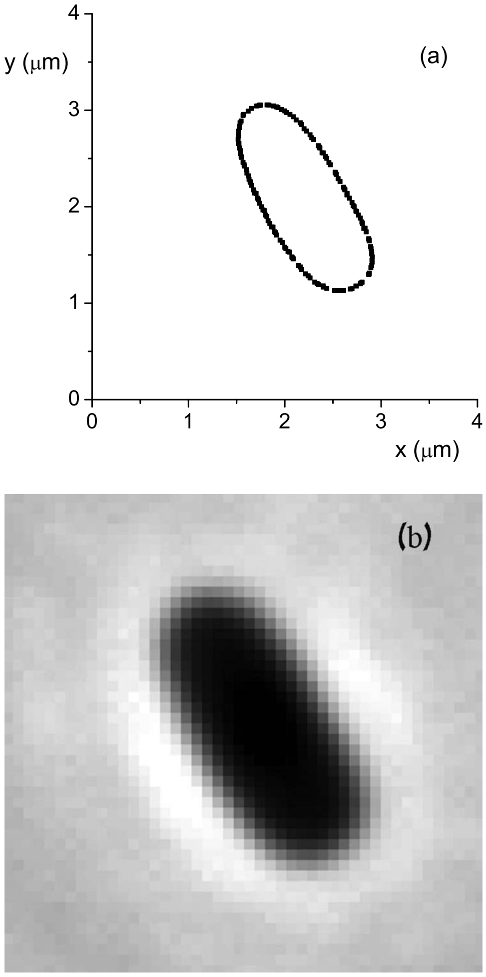

FIG. 3. A *fat* (bi-convex) bacterium. (a) The fluorescence contour, $\mathcal{C}_{\text{fl},1}$ (squares); (b) the corresponding phase contrast image. (a) and (b) have the same scale and origin.

The cells shown in Figs. 3–5 are extreme cases. Visual inspection would lead to the conclusion that a large fraction of the cells are well described by the rod shape. However, the high precision of our analysis reveals that, in fact, most cells deviate slightly from this shape.

On average, there are 200 data points in each cell contour. We aim to parametrize these contours using the simplest curve that retains the left-right asymmetry. The curvatures of the cell long sides that are related to breakdown of the cylindrical symmetry will be analyzed separately, as a second-order effect.

A. Parametrization of bacterial contours

To each of the cell contours, $\mathcal{C}_{\text{fl},1}$, we fit a shape, $\mathcal{C}_P$, that consists of straight lines on the long sides of the cell and circular arcs at the caps (see Fig. 6; the subscript P stands for "parts"). The corners, namely the four contour points $\mathbf{r}_1$, $\mathbf{r}_2$, $\mathbf{r}_3$, and $\mathbf{r}_4$, corresponding to the transition between the arcs and the lines, are chosen among seven neighboring candidates so as to minimize the χ^2 function. This minimization of

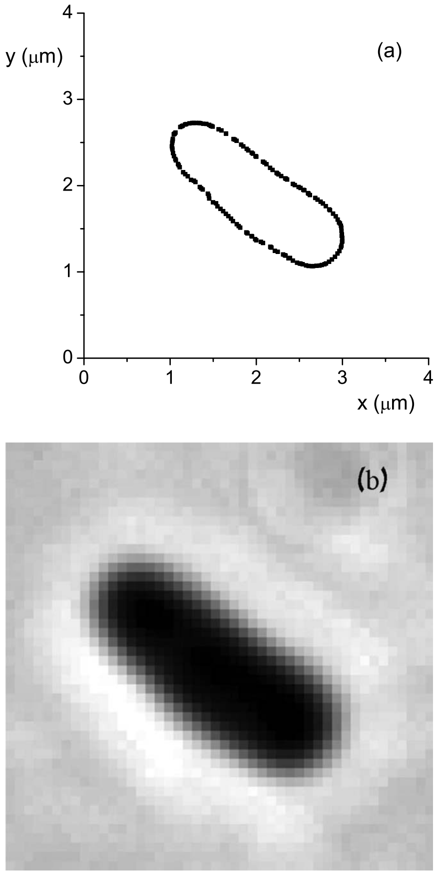

FIG. 4. Same as in Fig. 3 for a *half-fat* bacterium (plano-convex). The weak concave curvature of the upper long side is smaller than experimental error. This side qualifies as straight in our shape classification (see text).

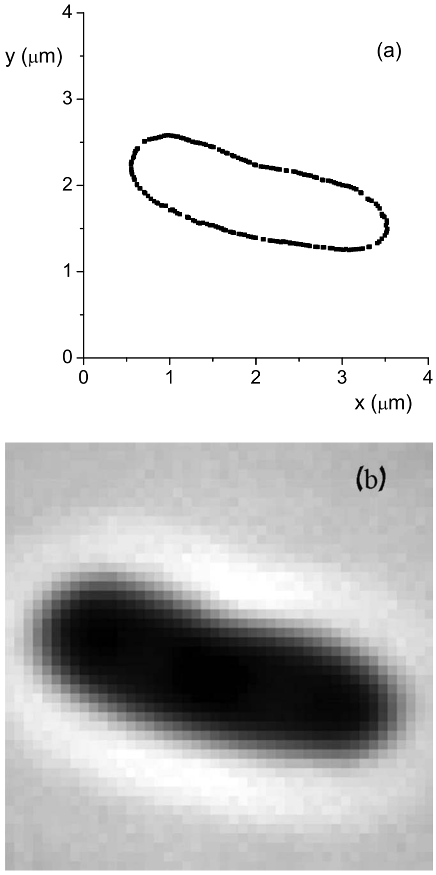

FIG. 5. Same as in Figs. 3 and 4 for a *banana* bacterium (convex-concave).

χ^2 is performed over all 7^4 combinations of candidate corners. We count the corners clockwise starting from the one with the lowest value of x, $x_1 < x_i$ for $i=2,3,4$. For comparison, we also fit to the contours the rod shape that consists of two semicircles with the same radius connected by two parallel lines, $\mathcal{C}_R$ (see Fig. 7; the subscript R stands for "rod").

Since both $\mathcal{C}_P$ and $\mathcal{C}_R$ are only defined over a limited x interval, we use a generalized form of the χ^2 function,

$$\chi^2 = \sum_{i=1}^{N} \frac{d_i^2}{\Delta^2}, \tag{4}$$

where i runs over the N contour points, d_i is the distance between the ith point and the $\mathcal{C}_P$ or $\mathcal{C}_R$ curve, and Δ is the average experimental error when measuring the location of a contour point (see Sec. II).

The $\mathcal{C}_R$ curve is uniquely determined by five parameters: the radius of the caps, R, the total length, L, the coordinates of the center of mass, and the orientation angle. On the other hand, $\mathcal{C}_P$ depends on ten parameters not including the freedom in locating the four corners. It is therefore not surprising that the cell contours are, on average, better approximated by the best-fitting $\mathcal{C}_P$ than by the corresponding $\mathcal{C}_R$. This is illustrated by the respective values of the χ^2 function. Averaging over 100 cells, we obtain $\langle\chi^2\rangle = 351.94$ for the best-fitting $\mathcal{C}_R$ and $\langle\chi^2\rangle = 138.76$ for $\mathcal{C}_P$. However, using the distribution of χ^2, one can also account for the different number of parameters between $\mathcal{C}_R$ and $\mathcal{C}_P$ using the confidence level (CL). This is defined as the probability that the theoretical curve provides the correct interpretation of the experimental results. The average confidence levels for the best-fitting $\mathcal{C}_R$

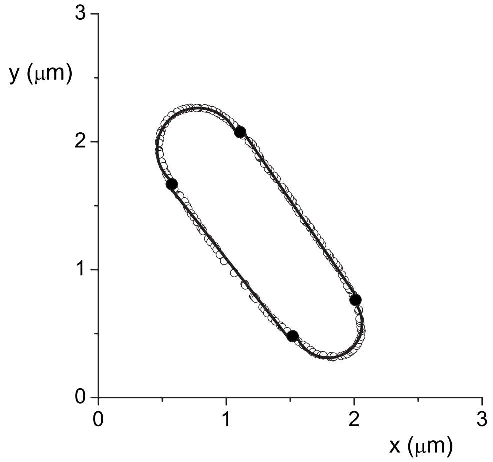

FIG. 6. The fluorescence contour of a bacterium, $\mathcal{C}_{\mathrm{fl},1}$, (open circles) is shown together with the corresponding best-fitting $\mathcal{C}_P$ shape (line). The full circles indicate the corners, $\mathbf{r}_1$, $\mathbf{r}_2$, $\mathbf{r}_3$, and $\mathbf{r}_4$, where the circular caps join the straight sides.

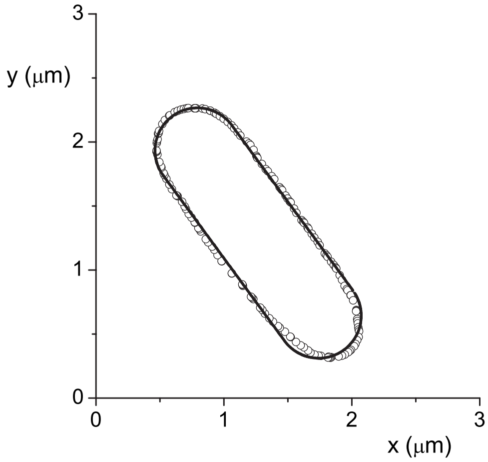

FIG. 7. Same as in Fig. 6, only here the best-fitting rod shape, $\mathcal{C}_R$, is shown (line).

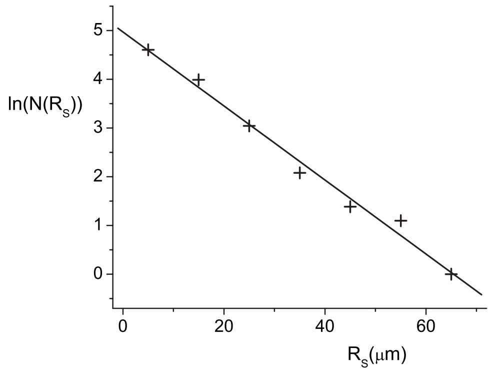

FIG. 8. The distribution of the radii of curvature, R_S, of the long sides for 100 *E. coli* cells (plusses). The bins of the histogram are 10 μm wide. On the y axis, we plot $\ln[N(R_S)]$, where $N(R_S)$ is the number of curvatures in the corresponding bin. The corresponding best-fitting straight line is also shown (line).

and $\mathcal{C}_P$ are $\mathrm{CL}_R=0.0758$ and $\mathrm{CL}_P=0.885$, respectively, indicating that the rod shape, $\mathcal{C}_R$, represents a significantly less adequate description of the *E. coli* cell shape than $\mathcal{C}_P$.

B. The left-right asymmetry of *E. coli*

The best-fitting $\mathcal{C}_P$ curve can be used to obtain a quantitative characterization of the deviations of the cell contour from the rod shape. First, we define a measure of the left-right asymmetry, A_{RL}, as

$$A_{RL}=\frac{R_1}{R_2}, \tag{5}$$

where R_1 and R_2 are the larger cap radius and the smaller one, respectively. Averaging over our cell population, we obtain $\langle A_{RL}\rangle=1.24$ and $\mathrm{Sd}(A_{RL})=0.16$. The corresponding coefficient of variation (CV) is $\mathrm{CV}_{RL}=0.13$. Not only does the average A_{RL} significantly differ from unity, but also its variability is large. To illustrate this, we have performed a numerical simulation in which rod-shaped contours are distorted by random noise of the size of our experimental error. Contour points were generated along the $\mathcal{C}_R$ of length and width equal to the corresponding average values measured in our cell population. Then, each such contour point is displaced in the direction perpendicular to $\mathcal{C}_R$ by a random amount, Δr, which is normally distributed with a standard deviation of 22 nm. We computed the values of A_{RL} for 30 such distorted $\mathcal{C}_R$ contours and found that $\langle A_{RL}\rangle=1.03$ and $\mathrm{Sd}(A_{RL})=0.02$ (with a CV of 0.019). This indicates that the left-right asymmetry in our cell population is significantly larger than that due to experimental error.

C. The cylindrical asymmetry of *E. coli*

In addition to the left-right asymmetry, the cells also appear to have slightly curved sides. This feature is ignored in both $\mathcal{C}_R$ and $\mathcal{C}_P$ parametrizations. In principle, one may use a curve that is more accurate in describing the observed cell shapes, e.g., a curve that consists of four separate circular arcs. Since two of these arcs have typically very large radii, a direct fit turned out to be difficult. Instead, we have approximately measured the curvatures of the cell sides using a simple geometrical construction. For each arc we use its edge points, A_R and A_L, and its middle point, A_C, to define two chords, A_RA_C and A_CA_L. From the middle of each chord we raise a perpendicular, L_R and L_L, respectively. The center of the circle that approximates the corresponding side of the cell lies at the intersection of L_R with L_L. We define the radius of this circle, R_S, as the average distance between the center of the circle and points A_R, A_C, and A_L. We find that $\langle R_S\rangle=19.80\ \mu\mathrm{m}=7.31\langle L\rangle$ and $\mathrm{Sd}(R_S)=33.66\ \mu\mathrm{m}=12.43\langle L\rangle$, where $\langle L\rangle$ is the average cell length. Although $\langle R_S\rangle$ is quite large, it is significantly smaller than the value due to experimental error, $\langle R_S\rangle=50.53\ \mu\mathrm{m}=18.66\langle L\rangle$. The curvature due to experimental error is obtained using the same numerical model as in the previous section. That is, we add Gaussian random noise with Sd=22 nm to the rod-shaped contour, $\mathcal{C}_R$, and measure the corresponding radius of its sides. Since the average radius of curvature obtained from the simulation is much larger than the one measured in the experiment, we may conclude that the long sides of cells are indeed curved.

The cells of the plano-convex type have one side with a very large radius of curvature, which, in turn, can have a large effect on the value of the measured $\langle R_S\rangle$. We find that the average cell curvature

$$C\equiv\frac{1}{2}\left(\frac{1}{R_{S,1}}+\frac{1}{R_{S,2}}\right), \tag{6}$$

where $R_{S,1}$ and $R_{S,2}$ are the radii of curvature of the two long sides, represents a more robust characterization of the cylindrical section cell curvature. For our population, we find $\langle C\rangle=0.125$ and $\mathrm{Sd}(C)=0.046$.

D. Curvatures of the long cell sides

In order to characterize the variability of cell shapes, we need more detailed information than just the averages of the various shape parameters. Therefore, for the case of the radii of curvature of the long cell sides, R_S, we show the probability distribution of the measured values (see Fig. 8). Despite the limited statistics, we find good agreement with an exponential distribution. This suggests there might be a random

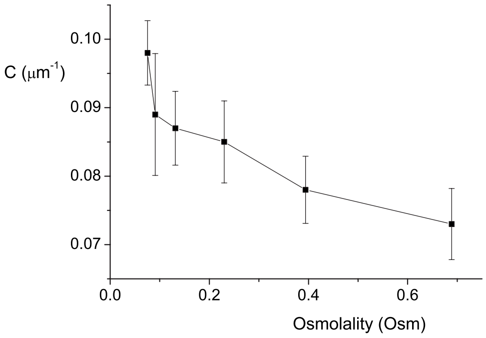

FIG. 9. Variation of the average cell curvature of the long sides with osmolality in osmotic shock experiments. Cells were grown in LB with 10 g/L NaCl corresponding to 0.394 Osm and then were moved to a new medium of varying osmolality that is shown on the *x* axis. The corresponding average cell curvature was measured and is displayed on the *y* axis (squares). The lines connecting the data points are only shown in order to guide the eye.

component in the mechanism that underlies the formation of these curvatures. It is possible that this randomness is linked to the random distribution of growth patches in the peptidoglycan cell wall.

A related measure of the shape variability is the classification into one of the three categories described before, namely bi-convex, plano-convex, and concave-convex. The radius of curvature for some of the cells is large and might be the result of measurement error. We therefore define as curved only cell sides for which R_S is smaller than the average value obtained from the distorted $\mathcal{C}_R$ simulation. In principle, a fourth cell type could be observed, namely cells that within experimental error have straight long sides. We find that our population consists of 85 bi-convex cells, 12 plano-convex, 3 concave-convex and none that are straight.

The small fraction of *banana*-shaped cells suggests that there may be more than a single mechanism that participates in determining the *E. coli* cell shape. That is, peptidoglycan growth at centers that are randomly distributed over the cylindrical section of the cell surface may be not sufficient to explain the observed cell shapes. As discussed in the Introduction, the MreB helix represents a second potential candidate to control the geometry of cells. Our analysis does not provide new information on the role of the MreB. It may, however, test whether a third factor, namely turgor pressure, also has an effect on *E. coli* cell shape. To this end, we have characterized the side curvature of cells grown in osmotic shock experiments. Live cells that grew in LB with 10 g NaCl/L were moved to a different medium with salt concentrations varying from 0 to 20 g/L. The change of medium was done at $\mathrm{OD}_{600}=0.2$ and imaging was performed right afterwards (within about 1 min). The analysis of the curvatures was done using only phase-contrast images. Although the experimental error is large, we find that the average curvature of the long cell sides, C, decreases with the osmolality of the medium (see Fig. 9). An even faster decrease of C with increasing osmolality was also observed for cells grown in LB with 0.5 g NaCl/L (not shown). In this case, however, when the LB shock medium contained 20 g/L NaCl, we found that cells were already plasmolyzed.

The main effect of increasing the osmolality of the medium is a corresponding decrease in the turgor pressure, P_t [13]. For the range of osmolalities of Fig. 9, P_t varies from ~2.5 atm to ~0.5 atm. Our results suggest that P_t has its own effect on the *E. coli* cell shape in addition to that of peptidoglycan growth and the helical MreB structure.

We have also tested the behavior of the average curvature for cells grown in LB media with different osmolalities. For the same range of osmolalities as that used in the shock experiments, we found no systematic trend for C. However, we find that other cell characteristics, e.g., the average length, $\langle L\rangle$, also vary with the osmolality. In this sense, in regular growth experiments more than one cell parameter is varied and each of these has a different influence on cell curvature. On the other hand, in shock experiments most cell parameters cannot significantly change over a 1 min time scale. As a result, in such experiments the effect of osmotic pressure on C is measured while all the slow varying cell parameters are frozen.

IV. CONCLUSIONS

We have obtained the contours of nonseptated *E. coli* cells with high precision and have analyzed their shape. We find that these contours deviate from the rod shape. The contours were shown to have asymmetric caps. Moreover, their sides are weakly curved. In individual cells these features may be more or less pronounced leading to shape variability over the bacterial population. We found that most of the cells have convex-shaped long sides. Only 3% of the cells were banana-shaped. Moreover, the radii of curvature for the long sides are Poisson distributed. Finally, in osmotic shock experiments, we find that the average curvature of the long sides decreases as the osmolality of the shock medium is increased. No clear trend was found for cells grown in media of varying osmolalities. These results suggest that in addition to the growth of peptidoglycan at randomly distributed loci and the effect of the MreB helices, the turgor pressure also plays a role in determining the precise shape of the *E. coli* cell.

Our findings raise several important questions. It was recently shown that *E. coli* cells are also functionally asymmetric, namely new caps behave differently from old ones [19]. Moreover, the cumulative age of the cap is a determining factor for the rate of growth over as much as nine generations. It may be that the age difference between the caps will also manifest as a difference in their respective geometries.

Symmetry also plays a role in bacterial division. *E. coli* divide at the center with an accuracy of about 4% [20,21]. It was shown that this accuracy is achieved by the joint action of the MinCDE system [22,23] and the nucleoid occlusion mechanism [24–27]. On the other hand, it is the 4% asymmetry in cell division that develops into the length variability of the bacterial population. It is possible that the asymmetry in the location of the septum correlates with the shape asymmetries of the cell prior to division.

In order to test these correlations, one should monitor the dynamics of the cell contours over several generations. Using fluorescent stains or GFP labeling of the membrane is not the most convenient approach. Most such labels distort to some extent the life cycle of the cell and/or its shape. Moreover, bleaching typically prevents sampling the dynamics at small enough time intervals. On the other hand, our approach allows one to use the phase-contrast contours, $\mathcal{C}_{\mathrm{ph},1}$, that were found to be almost as accurate as the fluorescence contours, $\mathcal{C}_{\mathrm{fl},1}$. In particular, the error of the $\mathcal{C}_{\mathrm{ph},1}$ contour point is only 31 nm. Such dynamic study will be presented in a subsequent publication.

ACKNOWLEDGMENTS

We thank Y. Meir, E. Moses, and A. Zaritsky for useful discussions, G. Reshes and S. Vanounou for help on some technical aspects of microscopy, and B. Pinshow for the measurements of osmolality that were done in his lab. This research was supported in part by grants from the Dean of Natural Sciences at Ben Gurion University and the Vice President for Research at Ben Gurion University.

---

[1] X. Yao, M. Jericho, D. Pink, and T. Beveridge, J. Bacteriol. **181**, 6865 (1999).
[2] A. L. Koch, Adv. Microb. Physiol. **24**, 301 (1983).
[3] A. L. Koch and M. F. S. Pinette, J. Bacteriol. **169**, 3654 (1987).
[4] M. Arnoldi, M. Fritz, E. Bauerlein, M. Radmacher, E. Sackmann, and A. Boulbitch, Phys. Rev. E **62**, 1034 (2000).
[5] N. Nanninga, Microbiol. Mol. Biol. Rev. **65**, 319 (2001).
[6] W. Vollmer and J.-V. Höltje, Curr. Opin. Microbiol. **4**, 625 (2001).
[7] T. den Blaauwen, M. E. G. Aarsman, N. O. E. Vischer, and N. Nanninga, Mol. Microbiol. **47**, 539 (2003).
[8] M. A. de Pedro, C. Quintela, J.-V. Höltje, and H. Schwarz, J. Bacteriol. **179**, 2823 (1997).
[9] M. A. de Pedro, H. Schwarz, and A. L. Koch, Microbiology **149**, 1753 (2003).
[10] T. J. Dougherty, K. Kenedy, R. E. Kessler, and M. J. Pucci, J. Bacteriol. **178**, 6110 (1996).
[11] R. Carballido-Lopez, Microbiol. Mol. Biol. Rev. **70**, 888 (2007).
[12] Y. Shih, T. Le, and L. Rothfield, Proc. Natl. Acad. Sci. U.S.A. **100**, 7865 (2003).
[13] D. S. Cayley, H. J. Guttman, and M. T. Record, Biophys. J. **78**, 1748 (2000).
[14] W. W. Baldwin and H. E. Kubitschek, J. Bacteriol. **159**, 393 (1984).
[15] W. W. Baldwin, M. J.-T. Sheu, P. W. Bankston, and C. L. Woldringh, J. Bacteriol. **170** 452 (1988).
[16] G. Carmon, N. Mamman, and M. Feingold, Physica A **376**, 117 (2007).
[17] G. Reshes, S. Vanounou, I. Fishov, and M. Feingold, Biophys. J. **94**, 251 (2008).
[18] K. A. Ross and M. G. Scanlon, J. Texture Stud. **30**, 17 (1999).
[19] E. J. Stewart, R. Madden, G. Paul, and F. Taddei, PLoS Biol. **3**, 295 (2005).
[20] N. B. Grover and C. L. Woldringh, Microbiology **147**, 171 (2001).
[21] L. J. H. Koppes, C. L. Woldringh, and N. Nanninga, J. Bacteriol. **134**, 423 (1978).
[22] P. A. J. de Boer, R. E. Crossley, and L. I. Rothfield, Cell **56**, 641 (1989).
[23] J. Lutkenhaus and M. Sundaramoorthy, Mol. Microbiol. **48**, 295 (2003).
[24] E. Mulder and C. L. Woldringh, J. Bacteriol. **171**, 4303 (1989).
[25] C. L. Woldringh, E. Mulder, J. A. C. Valkeburg, F. B. Wientjes, A. Zaritsky, and N. Nanninga, Res. Microbiol. **141**, 39 (1990).
[26] X. C. Yu and W. Margolin, Mol. Microbiol. **32**, 315 (1999).
[27] A. Rabinovitch, A. Zaritsky, and M. Feingold, J. Theor. Biol. **225**, 493 (2003).